

Electronic Supplementary Information of

Unexpected Phase Selectivity in Germanosilicate Zeolite Synthesis: Discovery and Structure of HPM-18, a Novel Stable d4r-Containing Structure

Huajian Yu,^{a,b} Zhenghan Zhang,^c Jian Li,^c Salvador R. G. Balestra,^d Zihao Rei Gao,^{*a,e} Miguel A. Camblor^{*a}

Table of Contents

| Title | Sub-title | Page |
|--------------------------------|---|------|
| Experimental Procedures | | 3 |
| | OSDA synthesis | 3 |
| | Zeolite synthesis | 3 |
| | Physicochemical characterizations | 3 |
| | Continuous Rotation Electron Diffraction (cRED) Data Collection | 3 |
| | Calculations | 3 |
| Supporting Figures | | 7 |
| Figure S1 | Projection of 3D reciprocal space reconstructed from cRED datasets of HPM-18 with $Ge_f = 0.8$. | 7 |
| Figure S2 | Projection of 3D reciprocal space reconstructed from cRED datasets of HPM-18 with $Ge_f = 0.8$, showing streaks indicative of structural disorder. | 7 |
| Figure S3 | Projection of 3D reciprocal space reconstructed from cRED datasets of HPM-18 with $Ge_f = 0.6$, showing streaks indicative of structural disorder. | 8 |
| Figure S4 | Projection of 3D reciprocal space reconstructed from cRED datasets of HPM-18 with $Ge_f = 0.17$. | 9 |
| Figure S5 | Projection of 3D reciprocal space reconstructed from cRED datasets of HPM-18 with $Ge_f = 0.17$. No streaks were detected, indicating a high degree of order. | 9 |
| Figure S6 | PXRD patterns of the samples prepared at $Ge_f = 0.3$ in the gel. The numbers x, yd in the legend correspond to the water/T ratio and crystallization time, respectively. | 10 |
| Figure S7 | Half width at half maximum of the 3.3° peak of the SPXRD patterns as a function of the Ge_f . | 10 |
| Figure S8 | Rietveld refinement plot of HPM-18 with $Ge_f = 0.17$. | 11 |
| Figure S9 | SEM images of HPM-18 with the Ge_f written. The magnification is the same in all the images. | 12 |
| Figure S10 | Ar adsorption and desorption isotherm of HPM-18 with $Ge_f = 0.17$. | 13 |
| Figure S11 | Unit cell of the HPM-18-E structure, with two initial sets of rotations of the $134TMI^+$ cations in the pore. | 14 |
| Supporting Tables | | 15 |
| Table S1 | Synthesis result of 134-TMI. | 15 |
| Table S2 | Indexing results of the cRED data with P-1 space group. | 16 |
| Table S3 | cRED experimental parameters, crystallographic data, and structure refinement details of HPM-18 ($Ge_f = 0.17$). | 17 |
| Table S4 | Details of Rietveld refinement for calcined HPM-18 ($Ge_f = 0.17$). | 18 |
| Table S5 | Rietveld refined Si-O bond distances (\AA) for calcined HPM-18 ($Ge_f = 0.17$). | 19 |
| Table S6 | Rietveld refined bond angles ($^\circ$) for calcined HPM-18 ($Ge_f = 0.17$). | 19 |
| Table S7 | Enumeration of the 16 possible ordered polymorphs of HPM-18, their $d4r$ sequences and up and down symbols (columns 1-3), and their topological analysis (columns 4-5), resulting in five topologically different ordered polymorphs and their channel systems (columns 6-7). | 20 |
| References | | 21 |

Experimental Procedures

OSDA synthesis

The OSDA, 134TMI, was synthesized by a procedure similar to one previously reported.^[28] First, 9.14 g (1 eq, 111 mmol) 4-methylimidazole (TCI, 98%) and 49.57 g potassium carbonate sesquihydrate (2.7 eq, Aldrich, 99%) were added into 250 mL chloroform (Scharlau, HPLC grade) under magnetic stirring in an ice-bath. Then, 56.78 g (3.6 eq, 400 mmol) of iodomethane (Aldrich, 99%) was added into the solution dropwise before covering the whole system. After 5 days of reaction, inorganic salts were removed by filtration and the product was collected by evaporating the solvent. After washing with diethyl ether (Scharlau, *p.a.*, 100 mL twice), the 134TMI iodide salt was dried at 45 °C (yield: 76%). Liquid NMRs was used for purity determination: ¹H (300 MHz, D₂O) δ 8.44 (s, 1H), 7.05 (s, 1H), 3.72 (s, 3H), 3.65 (s, 3H) and 2.18 (s, 3H). ¹³C (75 MHz, D₂O) δ 135.68, 132.05, 120.04, 35.50, 33.00, 8.19.

For anion exchange 16.67 g (70 mmol) 134TMI iodide was dissolved in 300 mL water and contacted with 140 mL resin (Amberlite (TM) IRN78 OH, 1.1 meq/mL cation exchange capacity by wet bed volume). After magnetic stirring overnight, the solution was collected by filtration and the resin was washed with water until neutral pH. The OSDAOH (134TMI⁺OH⁻) was concentrated by roto-evaporation and the concentration of OSDAOH was determined by HCl titration.

Zeolite synthesis

The germanosilicate HPM-18 of low Ge content was synthesized from a gel with composition 0.5 OSDAOH: 0.5 HF: 0.85 SiO₂: 0.15 GeO₂: 2.5 H₂O. First, 47.1 mg (0.45 mmol) GeO₂ was dissolved in 3.41 g (1.5 mmol, [OH⁻] = 0.442 mmol/g) OSDAOH for a few hours hydrolysis. Then, 569 μ L (2.55 mmol) TEOS (tetraethylorthosilicate, Aldrich, 98%) was added into solution as silicon source and the mixture was stirred overnight for hydrolysis and ethanol and water evaporation. After that, 55 μ L HF (27.6 mol/L) was added before putting the mixture into an oven at 90 °C for drying. Once the gel reached the targeted H₂O/TO₂ ratio, monitored by weight, it was mixed as homogeneously as possible before transferring it to a Teflon liner. The autoclave was placed into an oven at 150 °C for 7 days for crystallization. The results of other experiments at varying Ge_f, H₂O/SiO₂, temperature and time are summarized in Table S1.

Physicochemical characterizations

Phase identification was checked from laboratory powder X-ray diffraction (PXRD) data collected in the 3-45° 2 θ range on a Bruker D8 Advance diffractometer (Cu K α radiation, λ = 1.5418 Å). Field emission scanning electron microscopy (FE-SEM) images and energy-dispersive X-ray spectroscopy (EDS) data using a Gemini XM2i detector were obtained in a FEI Nova NanoSEM 230 microscope. C, H, N elemental analysis was measured on a LECO CHNS-932 or in a Vario EL III elemental analyzers. Thermogravimetric/differential thermal analyses (TG/DTA) were performed on a TA SDT Q600 thermal analyzer (10°C/min, 100ml/min Air). Multinuclear (¹³C, ¹⁹F, ²⁹Si) solid-state NMR spectra were acquired in a Bruker AV 400WB spectrometer and the conditions have been reported elsewhere.¹⁷ Argon adsorption experiments were performed on an Autosorb iQ machine from Quantachrome Instruments at 87K and the specific surface area was calculated by the multipoint BET method (P/P₀ = 0.008-0.053) using the ASiQWin (version 5.23, Quantachrome Instruments).

Continuous Rotation Electron Diffraction (cRED) Data Collection

For cRED characterization, the as-synthesized powders were finely ground and dispersed in ethanol, followed by ultrasonic treatment for 5 minutes. A drop of the resulting suspension, containing HPM-18 nanocrystals, was then deposited onto a 3 mm copper grid coated with a carbon film. The grid was subsequently mounted on a Fischione 2550 cryo-transfer tomography holder (maximum tilt range $\pm 79^\circ$) and inserted into the transmission electron microscope (TEM) for data acquisition.

cRED experiments were conducted using a FEI Tecnai F20 TEM equipped with a DECTRIS QUADRO detector (512 \times 512 pixels, pixel size 75 μ m). During data collection, the TEM goniometer was continuously rotated, and selected-area electron diffraction (SAED) patterns were recorded in video mode from successive tilt angles using a SerialEM script. To reduce electron dose and prevent damage to the beam-sensitive zeolite crystals, a spot size of 5, a 50 μ m C2

condenser aperture, and a 1 μm selected-area (SA) aperture (matched to the crystal dimensions) were used. The beam current in SA mode was maintained at ~ 0.5 pA.

To optimize data quality, beam alignment was first performed, after which the crystal was carefully adjusted to the eucentric height for precise focusing and selection of an appropriate region for measurement. During continuous rotation, the eucentric height was actively corrected using the wobbler to minimize displacement. The single-axis rotational stability of the FEI TEM goniometer allowed for fully automated data collection, with only minor crystal drift (~ 200 nm) observed over the -50° to 50° tilt range. Data corresponding to three samples with $\text{Ge}_f = 0.17$, 0.6 and 0.8 were collected in order to investigate Ge-dependent disorder. SAED data are shown in Figures S1-S5.

Rietveld Refinement

Synchrotron powder X Ray diffraction (SPXRD) datasets of samples with $\text{Ge}_f = 0.17$, 0.3, 0.6 and 0.8 were collected in capillary mode at beamline bl04 (MSPD) in the Spanish synchrotron radiation source (ALBA) located in Cerdanyola del Vallès (Barcelona) using the MAD26 multicrystal detector and a wavelength of 0.49587 Å. The structure of the ordered low Ge_f HPM-18 was refined by the Rietveld method using TOPAS.^[40] The Ge/Si occupancies at different T sites were refined as free parameters during the Rietveld refinement, with the total Si/Ge ratio constrained to match the overall framework composition determined by EDS analysis ($\text{Ge}_f = 0.17$), while the Si/Ge occupancies at individual T sites were allowed to refine freely within the range of 0-1 to ensure chemical reasonableness. In addition, the corresponding T–O bond distances were correlated with the refined site occupancies as $1.61 \times \text{OccSi}_i + 1.72 \times (1 - \text{OccSi}_i)$, where OccSi_i is the occupancy of Si at site T_i . This treatment provided physically meaningful bond lengths and reliable occupancy values consistent with the overall framework composition. The resulting occupancies converged smoothly and yielded physically reasonable T-O bonds, indicating the reliability of the refined site occupancies.

Calculations

Structure generation and optimisations

To assess the relative stability of HPM-18 polymorphs and ITW zeolites with respect to quartz, we conducted a series of structural optimisations. These calculations were carried out using the General Lattice Program (GULP),^[49,50] in conjunction with the interatomic potential developed by Sastre & Gale.^[51] In addition, 1,3,4-trimethylimidazolium (134TMI⁺) cations were modelled using the Dreiding forcefield,^[52] for intra- and intermolecular interactions. Atomic charges for the OSDA molecules were obtained via the Qeq method,^[53] and scaled to a total charge of +1 to ensure electroneutrality and compatibility with the Sastre & Gale potential (*i.e.*, it is compensated by F^- anions with charge -e). All F^- anions are located in the middle of the $d4r$ units. 134TMI⁺ cations were loaded in the pore, close to the F^- anions. As the 134TMI⁺ cation lacks rotational symmetry, several rotational orientations were systematically tested to identify the lowest-energy configuration for each Si/Ge distribution (see Figure S11).

Initial structural models for the HPM-18 polymorphs were derived from the crystallographic data obtained via Continuous Rotation Electron Diffraction (cRED). In the case of the IW structure, we obtained the initial coordinates from the IZA database.

Structural relaxations were performed employing both the Broyden–Fletcher–Goldfarb–Shanno (BFGS) algorithm and the Rational Function Optimisation (RFO) method, ensuring reliable convergence towards the global energy minimum. Our procedure consisted of two sequential steps. Initially, atomic positions were optimised while maintaining both the unit cell volume and shape fixed. Subsequently, full relaxation of the cell parameters was performed using the BFGS algorithm. Once the gradient norm was below $0.3 \text{ eV } \text{\AA}^{-1}$, the minimiser was switched to RFO, with a final convergence criterion set at a gradient norm below $1 \times 10^{-5} \text{ eV } \text{\AA}^{-1}$. For the evaluation of interatomic forces, we applied a cut-off of 12 Å, and a shorter cutoff of 0.8 Å was adopted for harmonic bonds linking core and shell particles. This prevents shell–shell overlapping issues. All structures were optimised at 0 GPa without symmetry constraints, and both the lattice and atomic coordinates were allowed to relax freely (*i.e.* P1).

Si/Ge Site Occupancy Disorder

We employed the Site Occupancy Disorder (SOD) program,^[54,55] to systematically generate all symmetrically inequivalent configurations corresponding to the substitution of Si by Ge atoms at T-

sites within the unit cell of the **ITW** zeolite framework. We used the monoclinic space group $C12/m1$ (#12), as reported in the IZA database, which includes 3 crystallographically independent T-sites. The unit cell comprises 24 T-sites. Regarding the **HPM-18** structure, the experimental structure exhibits P-1 symmetry with 48 T atoms, as reported in the main text. However, just for the configurational modelling, we employed the higher-symmetry IZA-type $C2/c$ (#15) space group. This choice substantially reduces the combinatorial complexity and thus the number of non-equivalent Si/Ge distributions for the HPM-18-E polymorph. All structures were finally optimised without symmetry constraints, as mentioned above.

Although generating random structures for intermediate Ge_f values is straightforward in principle, establishing whether any of them is truly representative is considerably more challenging, because the number of accessible microstates is really huge. Initially, we worked close to both ends of the substitutional series, *i.e.* at low and high Ge contents. For ITW structures, for each substitution number $n_{Ge} = 0, 1, 2, 3, 4, 20, 21, 22, 23$, and 24, we generated all inequivalent configurations, obtaining respectively $m = 1, 3, 45, 253, 1386, 1386, 253, 45, 3$, and 1 configurations. This corresponds to a total of 3376 symmetrically inequivalent configurations, which were fully optimised following the protocol described above. Regarding the **HPM-18-E** structure, we applied the same protocol as used for ITW. We found that the number of inequivalent configurations increases *dramatically* for HPM-18. For example, for $n_{Ge} = 0, 1, 2, 3, 93, 94, 95$, and 96 substitutions, the corresponding numbers of inequivalent configurations are $m = 1, 12, 612, 17860, 17860, 612, 12, 1$, respectively. This indicates a much higher configurational entropy in HPM-18. All these structures were optimised using the Sastre & Gale potential.

So, for intermediate germanium molar fractions, we employed a statistical approach based on the methods introduced by Rigo *et al.* (2018),^[56] and Arce-Molina *et al.* (2018),^[57] which allows the reconstruction of energies at intermediate ranges using data from low and high mole fraction limits (the structures we have optimised previously):

Specifically:

- 1) We developed a custom version of the SOD algorithm (rewritten in FORTRAN and available at: <https://github.com/salrodgom/sod>) to generate a manageable ensemble of non-equivalent structures where exhaustive calculation is unfeasible.
- 2) Structures were ranked using the Arce-Molina estimator, which we modified to include up to 4-body cluster energy correction (this correction is particularly suitable for germanosilicates, where germanium atoms tend to site in *d4r* units, and other analogous structural motifs). This correction was necessary to achieve a high correlation between the estimated energy and the energy calculated using the Sastre & Gale potential (see Rigo *et al.*).
- 3) From this ranked list, a reduced ensemble of $N = 1000$ structures was selected for full geometry optimisation using GULP with the classic force field (at 0 GPa). The ensemble was selected using uniform probabilities and swapping between Si and Ge species. A Markov-chain Monte Carlo scheme is being prepared to future studies.
- 4) We estimated the averaged internal energy $\langle U \rangle \sim \langle E \rangle_N$ and its error within the ensemble using the variance $\langle E^2 \rangle_N - \langle E \rangle_N^2$.
- 5) The entropy was approximated as $S_{conf} = S_{mix} + S_{poly}$. A fully rigorous evaluation of vibrational entropy at the synthesis temperature ($T = 423.15$ K), although desirable, would have required an unfeasible number of phonon calculations. The configurational contribution was therefore decomposed in:

$$S_{conf} = S_{mix} + S_{poly},$$

Here, S_{mix} is the Si/Ge mixing entropy according to Grau-Crespo *et al.*, and S_{poly} is the configurational entropy associated with the coexistence of multiple HPM-18 polymorphs (A–E). For low Ge contents ($x_{Ge} \rightarrow 0$), the relative enthalpies of the five polymorphs (0, 0.14, 1.51, 2.79, 2.81 kJ mol⁻¹ per T-atom) yield a stabilisation $-TS$ of:

$$-T S(x_{Ge} \rightarrow 0)^{max}_{poly} \sim -5.45 \text{ kJ/mol (per T-atom)},$$

assuming random stacking (zero interlayer interaction) at the synthesis temperature. For high Ge contents ($x_{Ge} \rightarrow 1$), the corresponding values (0, 0.19, 0.66, 1.17, 1.41 kJ mol⁻¹ per T-atom) give us:

$$-T S(x_{\text{Ge}} \rightarrow I)_{\text{poly}}^{\text{max}} \sim -5.62 \text{ kJ/mol (per T-atom)}.$$

At this temperature, the enthalpic differences between polymorphs are minimal (e.g., E and D differ by only 0.14 kJ/mol), resulting in nearly identical probabilities. Even the less stable polymorphs (A and C) retain probabilities above 12 %. The system therefore exhibits no strong thermodynamic preference for a single structure, consistent with the emergence of extensive correlated disorder and the difficulty in isolating pure-phase crystals at high germanium contents. Importantly, this stabilisation (~ 5.5 kJ/mol) exceeds the full enthalpic spread between the most and least stable polymorphs (2.81 kJ/mol). This indicates that the disordered, mixed-polymorph state is thermodynamically more favourable than any ordered phase due to the substantial configurational entropy gain. This constitutes a clear example of entropy-driven stabilisation in zeolites.

Consequently, the formation Gibbs energy per T-atom relative to the quartz-type and OSDAF-type references is:

$$\langle \Delta g \rangle \sim (\langle E \rangle_N - T S_{\text{conf}}) / N_T - \langle g \rangle_{\text{quartz}},$$

being N the number of samples (configurations in the statistical ensemble) and N_T the number of T-atoms in the unit cell.

Reference structures

In order to evaluate the relative stability of the germanosilicate frameworks presented in this work (see Figure 5 and Table 2), the excess Gibbs energy per T-atom was calculated relative to a composition-weighted reference of the dense oxide phases. For silica (SiO_2), the reference state employed is α -quartz, which is the thermodynamically stable polymorph at ambient conditions. Since zeolites are four-coordinated frameworks, we have adopted the quartz-type GeO_2 polymorph (space group $P3_121$) as the reference state for the germanium component. This phase is tetrahedrally coordinated and isostructural with α -quartz SiO_2 , allowing for a direct and consistent comparison of framework energies across the entire composition range.

To define an appropriate reference state for stabilisation energies, we generated a hypothetical unit cell containing two 134TMI^+ cations and two fluoride anions and optimised it at the same level of theory. This allows us to report formation Gibbs energies relative to the occluded state rather than to the empty framework.

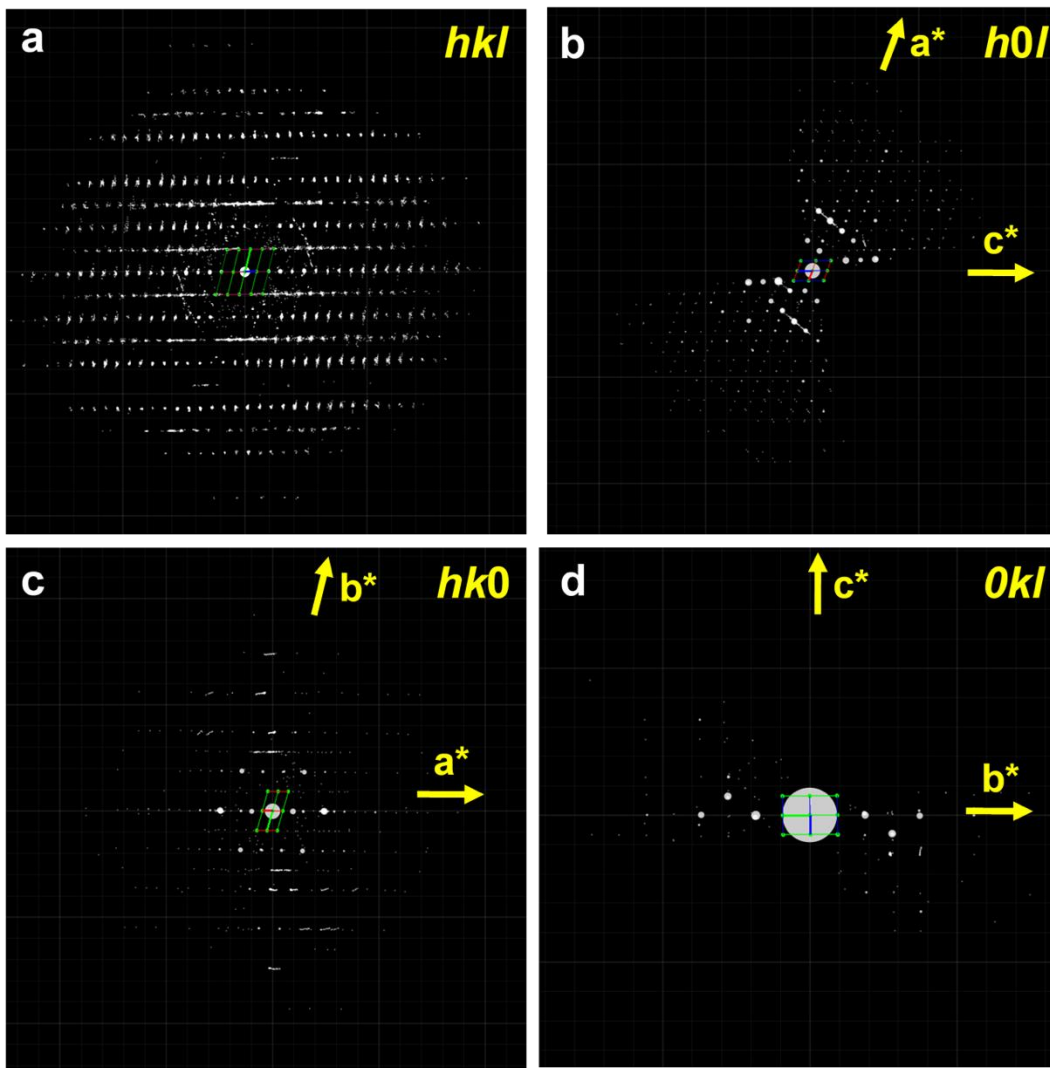


Figure S1. Projection of 3D reciprocal space reconstructed from cRED datasets of HPM-18 with $Ge_f = 0.8$.

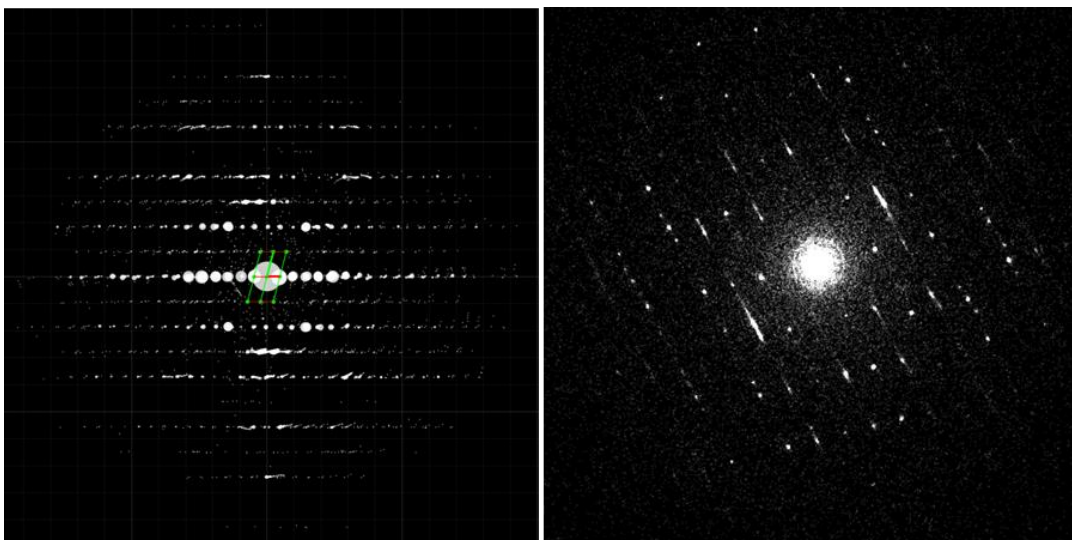


Figure S2. Projection of 3D reciprocal space reconstructed from cRED datasets of HPM-18 with $Ge_f = 0.8$, showing streaks indicative of structural disorder.

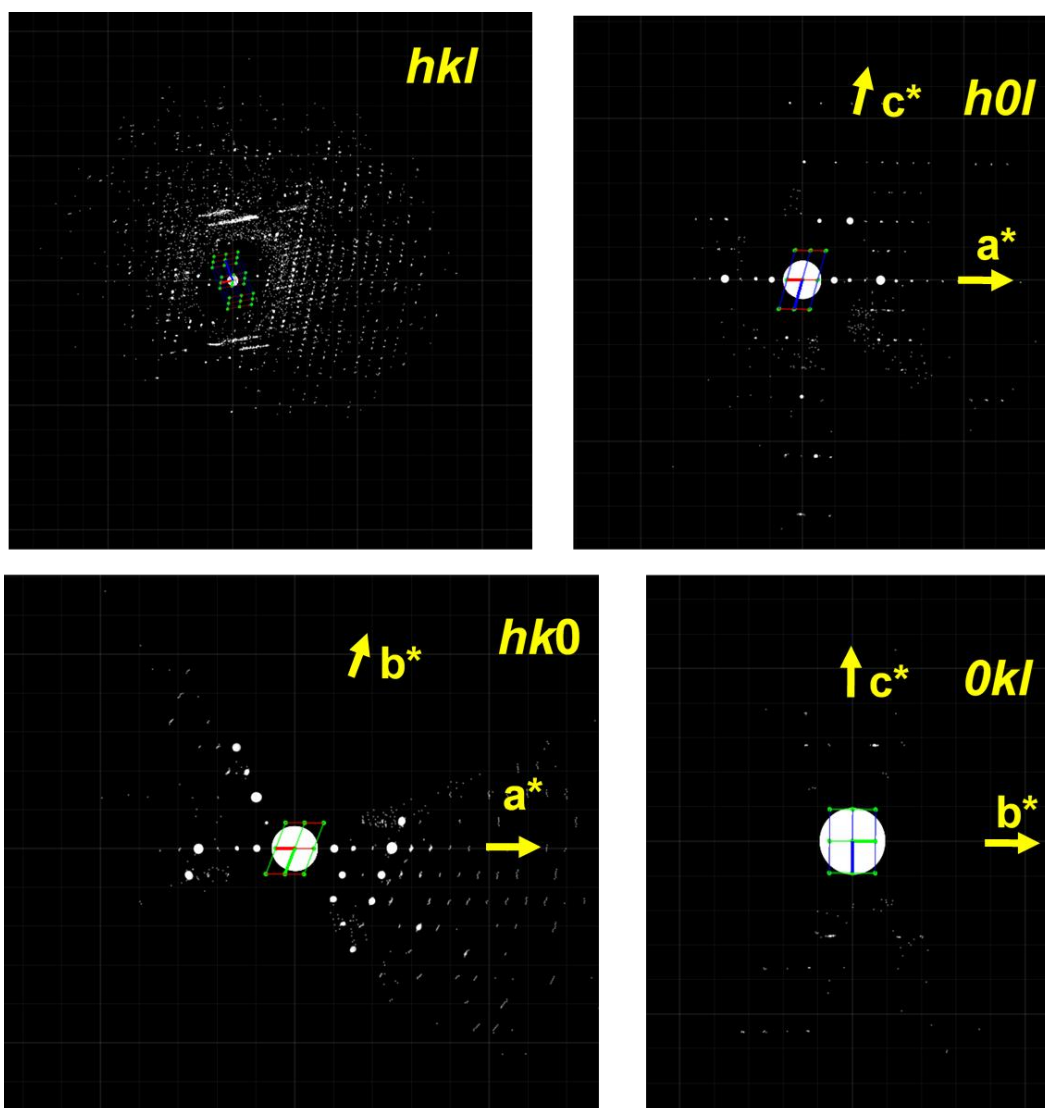


Figure S3. Projection of 3D reciprocal space reconstructed from cRED datasets of HPM-18 with $Ge_f = 0.6$, showing streaks indicative of structural disorder.

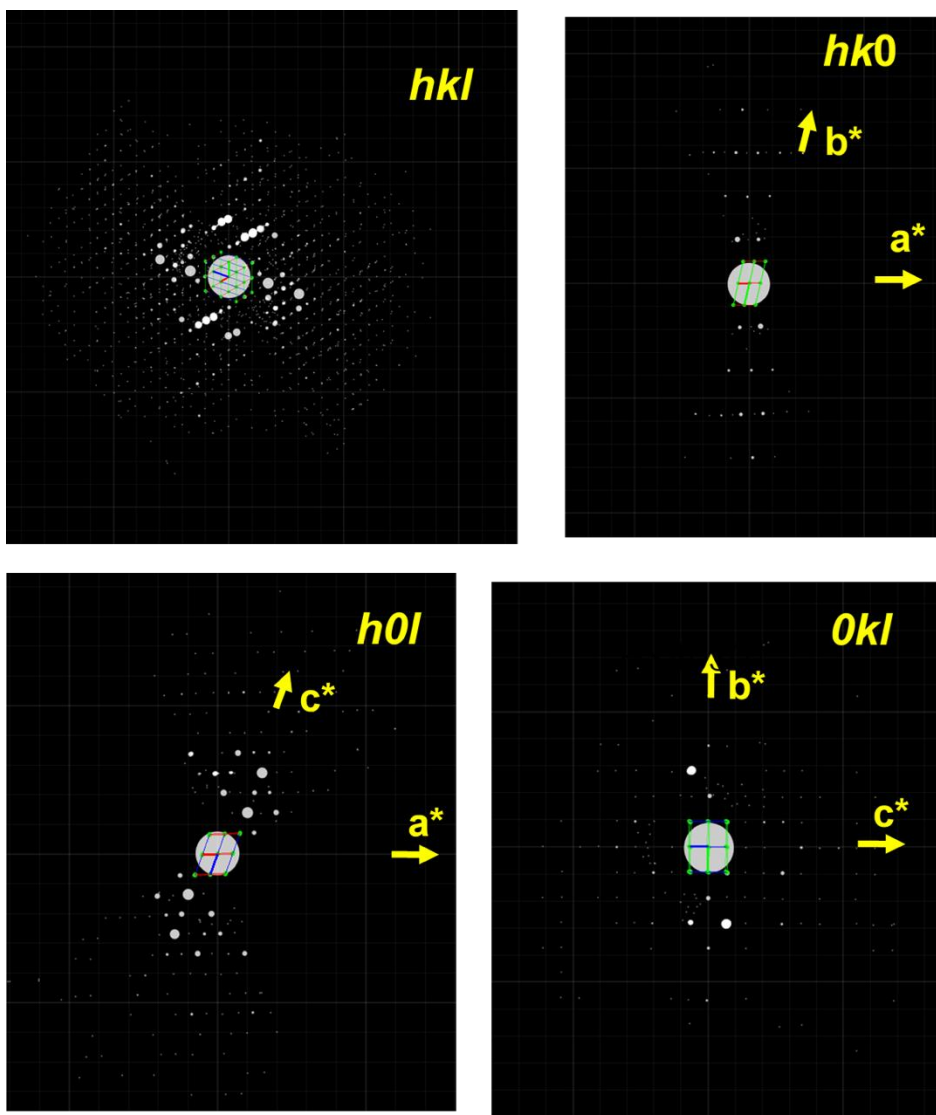


Figure S4. Projection of 3D reciprocal space reconstructed from cRED datasets of HPM-18 with $Ge_f = 0.17$.

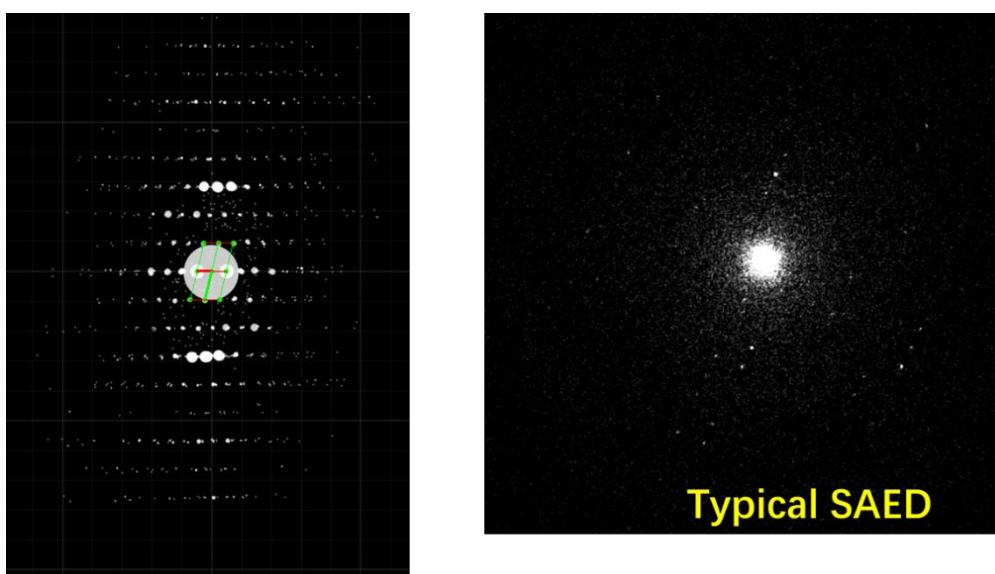


Figure S5. Projection of 3D reciprocal space reconstructed from cRED datasets of HPM-18 with $Ge_f = 0.17$. No streaks were detected, indicating a high degree of order.

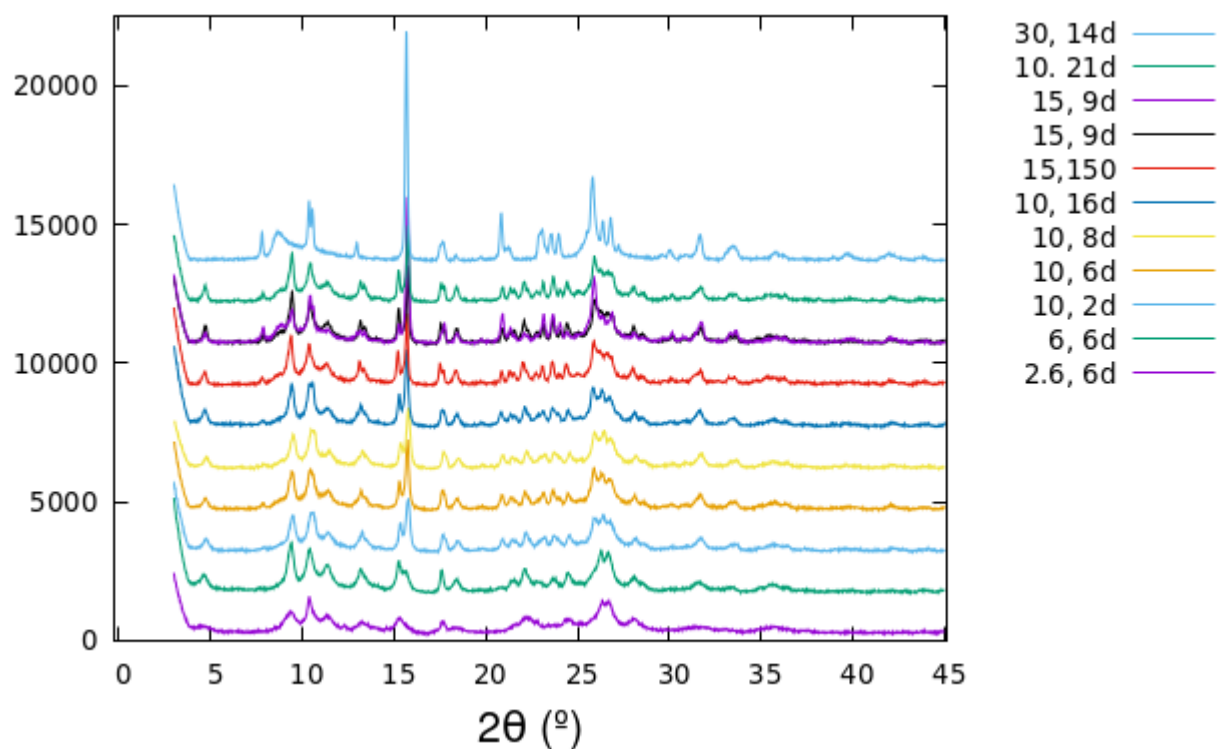


Figure S6. PXRD patterns of the samples prepared at $Ge_f = 0.3$ in the gel. The numbers x, yd in the legend correspond to the water/T ratio and crystallization time, respectively.

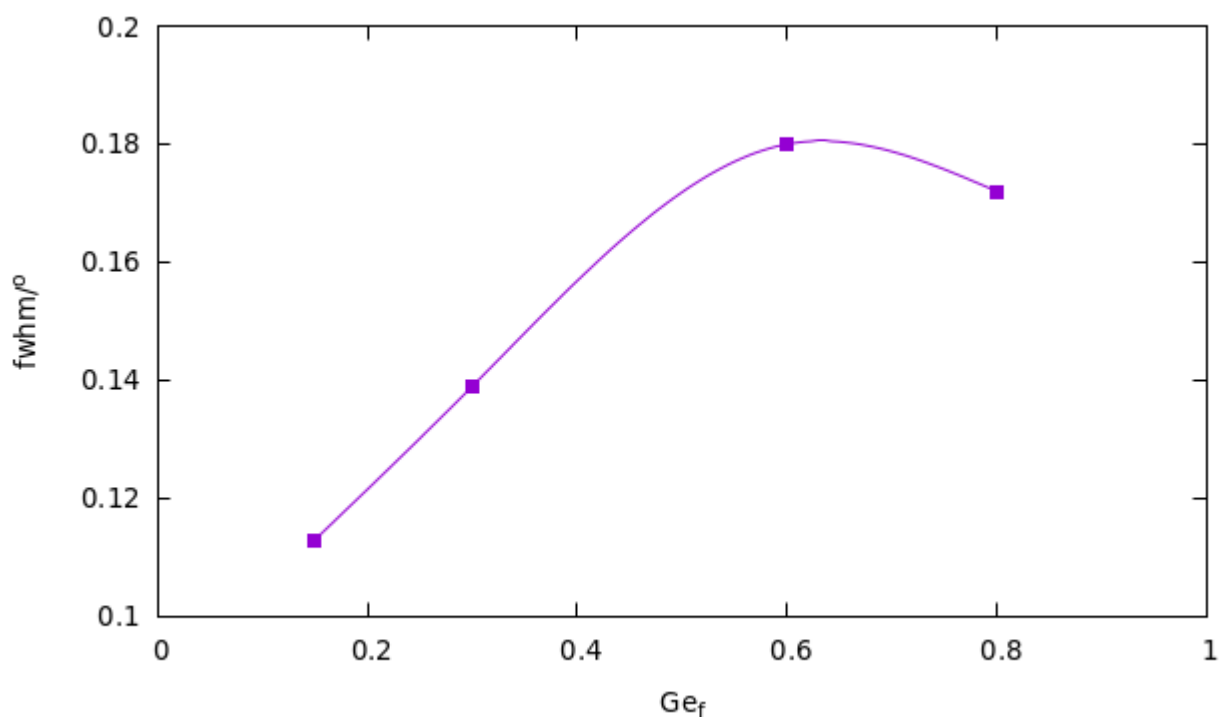


Figure S7. Half width at half maximum of the 3.3° peak of the SPXRD patterns as a function of the Ge_f .

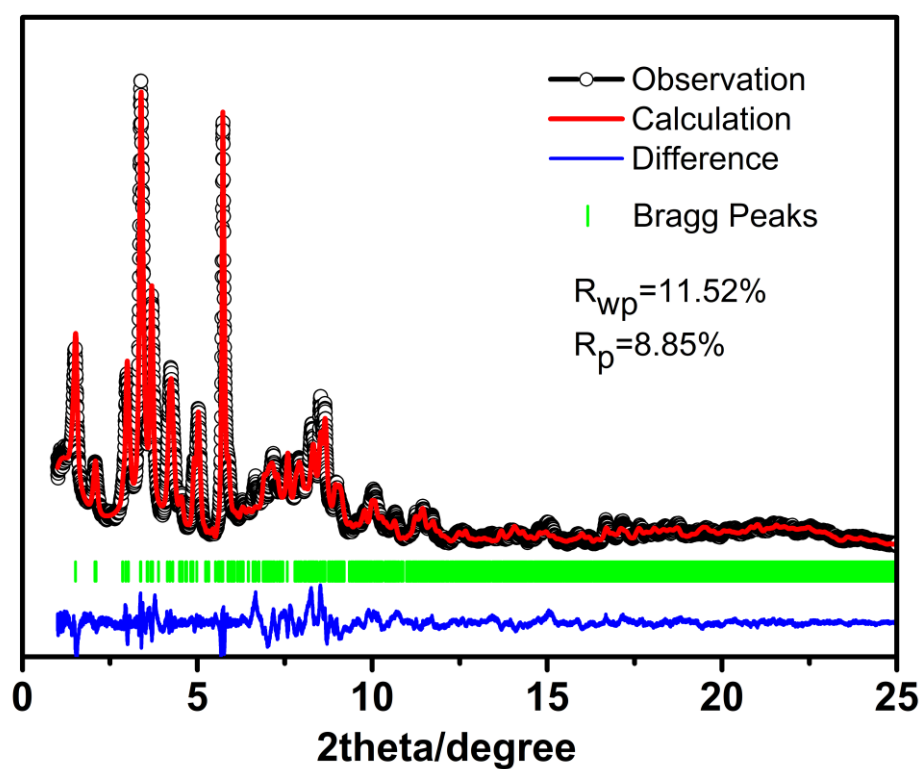


Figure S8. Rietveld refinement plot of HPM-18 with $Ge_f = 0.17$. Wavelength of 0.49587 Å.

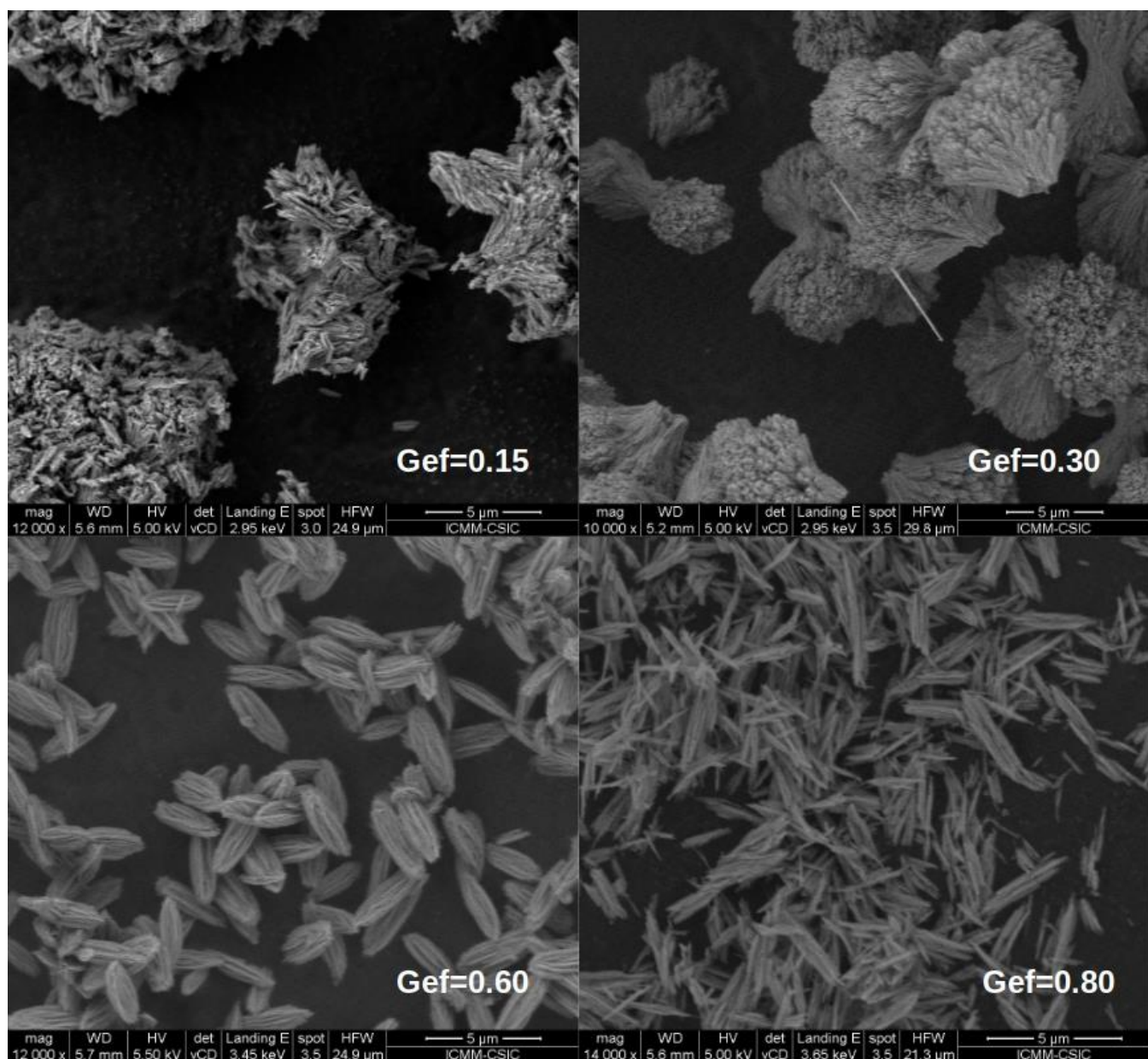


Figure S9. SEM images of HPM-18 with the Ge_f written. The magnification is the same in all the images.

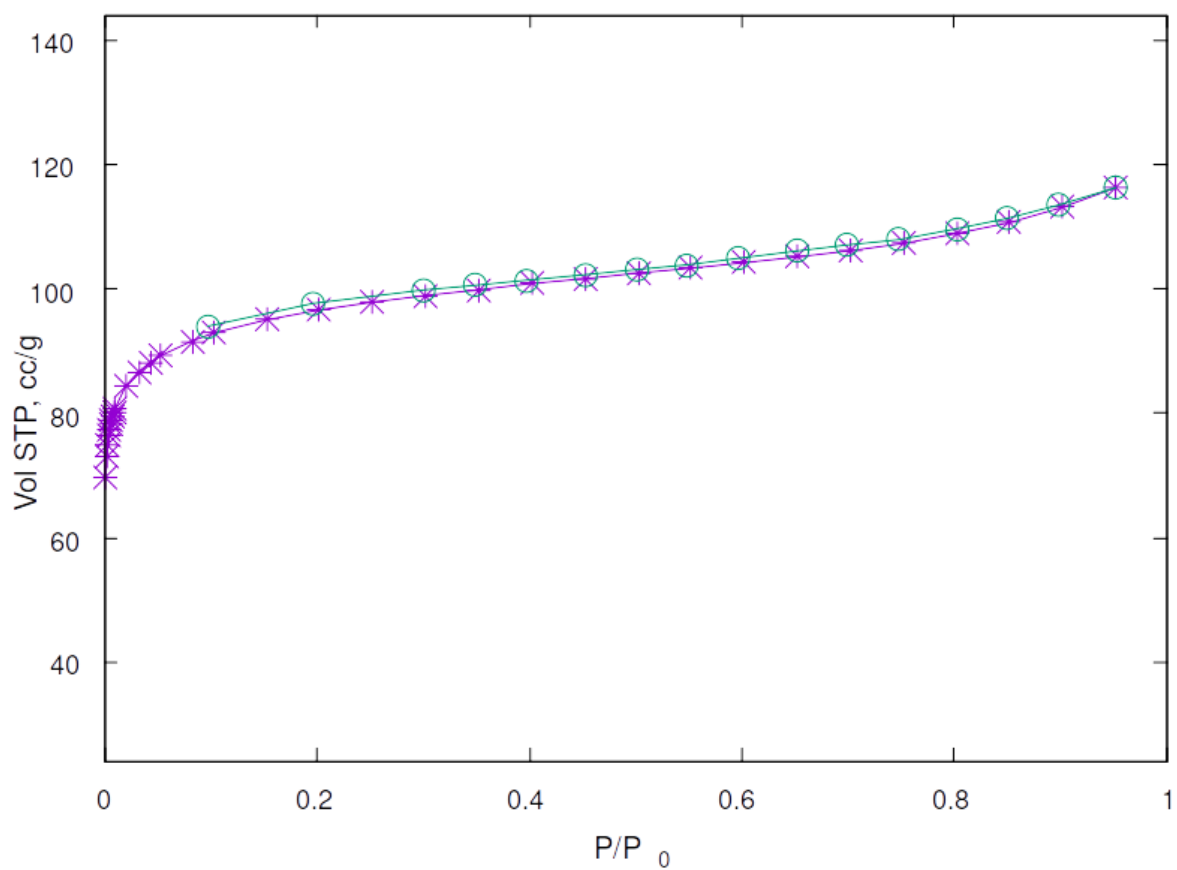


Figure S10. Ar adsorption (purple crosses) and desorption (green circles) isotherms of HPM-18 with $Ge_f = 0.17$.

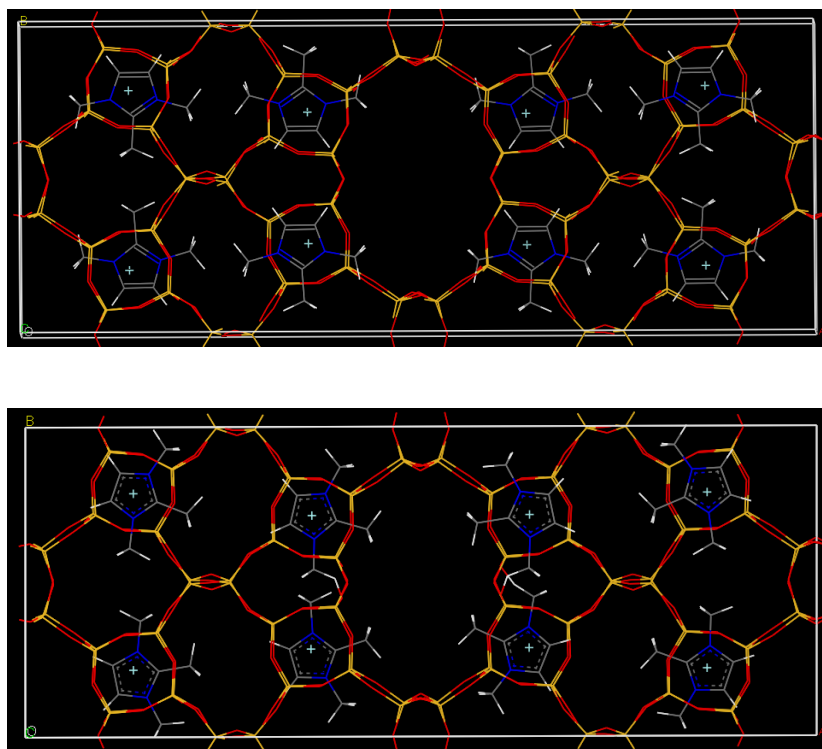


Figure S11. Unit cell of the HPM-18-E structure, with two initial sets of rotations of the 134TMI^+ cations in the pore.

Table S1. Synthesis result of 134-TMI.

| Ge _f | OSDA/T | H ₂ O/T | OH/F | T °C | Time | Stirring | XRD | | | | | |
|-----------------|--------|--------------------|------|--------|------------------|------------------|------------------|----------|--------|----------------|--------|----|
| 0.1 | 0.5 | 1 | 1 | 150 | 3d | Static | Am | | | | | |
| | | | | | 6d | Static | Am | | | | | |
| | | | | | 13d | Static | ITW+(HPM-18) | | | | | |
| | | 2.5 | 1 | 150 | 7d | Static | ITW | | | | | |
| | | | | 6 | 1 | 150 | 7d | Static | ITW | | | |
| | | 6 | 1 | 150 | 3d | Static | ITW | | | | | |
| | | | | 175 | 6d | Static | ITW | | | | | |
| | | | | 13d | Static | ITW | | | | | | |
| | | | | 14d | Static | ITW | | | | | | |
| | | | | 10 | 1 | 150 | 7d | Static | ITW | | | |
| | | | | 0.15 | 0.5 | 2.5 | 1 | 150 | 7d | Static | HPM-18 | |
| | | 6 | 1 | 150 | 7d | Static | ITW | | | | | |
| 0.2 | 0.5 | | | 2.5 | 1 | 150 | 7d | Static | Am | | | |
| 6 | 1 | 150 | 7d | Static | HPM-18 | | | | | | | |
| | | 0.3 | 0.5 | 2.5 | 1 | 150 | 6d | Static | HPM-18 | | | |
| 6 | 1 | 150 | 6d | Static | HPM-18 (+ IM-18) | | | | | | | |
| | | 10 | 1 | 150 | 2d | Static | HPM-18 + IM-18 | | | | | |
| | | | | | 6d | Static | HPM-18 + IM-18 | | | | | |
| | | | | | 8d | Static | HPM-18 + IM-18 | | | | | |
| | | | | | 16d | Static | HPM-18 + IM-18 | | | | | |
| | | | | | 15 | 1 | 150 | 4d | Static | HPM-18 + IM-18 | | |
| | | | | | 9d | Static | HPM-18 + IM-18 | | | | | |
| | | | | | 9d | Static | HPM-18 + IM-18 | | | | | |
| | | | | | 21d | Static | IM-18 + HPM-18 | | | | | |
| | | | | | 14d | Static | IM-18 | | | | | |
| | | | | | 0.6 | 0.5 | 2.5 | 1 | 150 | 6d | Static | Am |
| | | | | | 6 | 1 | 150 | 6d | Static | HPM-18 | | |
| 10 | 1 | 150 | 6d | Static | | | HPM-18 | | | | | |
| 0.8 | 0.5 | 4 | 1 | 150 | 4d | Static | HPM-18 | | | | | |
| | | | | | 10d | Static | HPM-18 | | | | | |
| | | | | | 6 | 1 | 150 | 2d | Static | HPM-18 | | |
| | | | | | | | 4d | Static | HPM-18 | | | |
| | | | | | | | 6d | Static | HPM-18 | | | |
| | | | | | | | 4d | Rotation | HPM-18 | | | |
| | | | | | | | 8d | Rotation | HPM-18 | | | |
| | | | | | | | 12d | Rotation | HPM-18 | | | |
| | | | | | | | 175 | 3d | Static | HPM-18 | | |
| | | | | | | | 6d | Static | HPM-18 | | | |
| | | | | | | | 15d | Static | HPM-18 | | | |
| | | | | | | | 45d | Static | HPM-18 | | | |
| | | 8 | 1 | 150 | 4d | Static | HPM-18 | | | | | |
| | | | | 10d | Static | HPM-18 | | | | | | |
| | | 10 | 1 | 150 | 6d | Static | HPM-18 | | | | | |
| | | | | 6d | Static | HPM-18 | | | | | | |
| | | | | 16d | Static | HPM-18 | | | | | | |
| | | 15 | 1 | 150 | 6d | Static | HPM-18 | | | | | |
| | | | | 10d | Static | HPM-18 | | | | | | |
| | | | | 16d | Static | HPM-18 | | | | | | |
| | | 0.8 | 6 | 1 | 150 | 4d | Static | HPM-18 | | | | |
| | | | | | 10d | Static | HPM-18 | | | | | |
| | | | | | 10d | Static | HPM-18 | | | | | |
| 1 | 0.5 | 6 | 1 | 150 | 2d | Static | GeO ₂ | | | | | |
| | | | | | 4d | Static | GeO ₂ | | | | | |
| | | | | | 6d | Static | GeO ₂ | | | | | |
| | | 15 | 1 | 150 | 5d | Static | GeO ₂ | | | | | |
| | | | | 8d | Static | GeO ₂ | | | | | | |
| | | 25 | 1 | 150 | 5d | Static | GeO ₂ | | | | | |
| | | | | 5d | Static | GeO ₂ | | | | | | |
| | | | | 8d | Static | GeO ₂ | | | | | | |

Table S2. Indexing results of the cRED data with P-1 space group.

| Dataset | Space Group | <i>a</i> /Å | <i>b</i> /Å | <i>c</i> /Å | <i>α</i> /° | <i>β</i> /° | <i>γ</i> /° | <i>V</i> /Å ³ | Rotation Angle/° | Completeness/% |
|---------|-------------|-------------|-------------|-------------|-------------|-------------|-------------|--------------------------|------------------|----------------|
| 1 | #2 | 21.3 | 10.7 | 14.9 | 90.4 | 109.5 | 104.8 | 3129.95 | 98.8 | 53.5 |
| 2 | #2 | 21.2 | 10.8 | 14.8 | 90.4 | 108.9 | 104.9 | 3098.23 | 98.5 | 54.4 |
| 3 | #2 | 21.2 | 10.82 | 15.1 | 89.9 | 109.1 | 105.4 | 3124.37 | 99.1 | 53.7 |
| 4 | #2 | 20.98 | 10.69 | 14.95 | 89.78 | 109.0 | 105.2 | 3046.72 | 73.4 | 26.3 |
| 5 | #2 | 21.03 | 10.79 | 14.77 | 89.9 | 108.7 | 105.1 | 3050.93 | 98.5 | 31.4 |
| 6 | #2 | 21 | 10.8 | 14.88 | 89.87 | 108.8 | 105.3 | 3066.30 | 64.9 | 20.2 |
| 7 | #2 | 21.12 | 10.77 | 14.88 | 90.27 | 108.8 | 105.1 | 3076.20 | 78.4 | 23.9 |
| 8 | #2 | 21.2 | 10.75 | 14.99 | 90.15 | 109.4 | 105.1 | 3095.38 | 88.8 | 27.2 |
| 9 | #2 | 21.2 | 10.79 | 14.95 | 90.17 | 109.4 | 104.9 | 3100.70 | 98.49 | 30.2 |

Table S3. cRED experimental parameters, crystallographic data, and structure refinement details of HPM-18 ($G_{\text{eff}} = 0.17$).

| | |
|--|---|
| Sample | HPM-18-ordered |
| No. of datasets | 9 |
| Wavelength | 0.0251 |
| Program for data proccession | XDS |
| Program for structure solution | <i>SHELXT</i> |
| Crystal system | triclinic |
| Unit cell dimensions | $a = 20.947(4) \text{ \AA}$ $b = 10.597(2) \text{ \AA}$ $c = 14.937(3) \text{ \AA}$ $\alpha = 90.50(3)^\circ$ $\beta = 110.30(3)^\circ$ $\gamma = 103.82(3)^\circ$ |
| Possible space group | <i>P</i> -1 |
| Resolution | 1.0 \AA |
| Completeness | 72.9% |
| R_{int} | 30.07% |
| No. of reflections | 14254 |
| No. of unique reflections | 4574 |
| Formula | $\text{Si}_{48}\text{O}_{96}$ |
| Crystal system | triclinic |
| Space group | <i>P</i> -1 |
| Unit cell dimensions | $a = 20.947(4) \text{ \AA}$ $b = 10.597(2) \text{ \AA}$ $c = 14.937(3) \text{ \AA}$ $\alpha = 90.50(3)^\circ$ $\beta = 110.30(3)^\circ$ $\gamma = 103.82(3)^\circ$ |
| $F(000)$ | 501 |
| Dataset (h, k, l) | -10~10, -14~14, -18~17 |
| Total data, unique data, R_{int} | 14254, 4574, 30.07% |
| Observed data [$F_0 > 4\text{sig}(F_0)$] | 1000 |
| No. of reflections, No. of parameters, No. of restraints | 4574, 293, 82 |
| R_1, wR_2, GoF | 24.04%, 55.34, 1.042 |
| I/σ | 2.5 |
| $\rho_{\text{min}}, \rho_{\text{max}}$ ($\text{e}^-/\text{\AA}^3$) | 0.2, -0.1 |
| CCDC | 2473072 |

Table S4. Details of Rietveld refinement for calcined HPM-18 ($\text{Ge}_f = 0.17$).

| | |
|--|--|
| Identification code | Calcined HPM-18 |
| Empirical formula | $\text{Si}_{39.92}\text{Ge}_{8.08}\text{O}_{96}$ |
| Wavelength | 0.49587 |
| Radiation | Synchrotron radiation |
| Crystal system | triclinic |
| Space group | $P\bar{1}$ |
| Unit cell dimensions | $a = 20.660(8)\text{\AA}$ |
| | $b = 10.299(3)\text{\AA}$ |
| | $c = 14.601(5)\text{\AA}$ |
| | $\alpha = 90.21(5)^\circ$ |
| | $\beta = 109.36(3)^\circ$ |
| Z | $\gamma = 104.66(5)^\circ$ |
| | 1 |
| 2θ range for refinement($^\circ$) | 1-25 |
| No. of parameters | 250 |
| No. of reflections | 3917 |
| No. of data points | 8000 |
| No. of restraints | 96 for Si-O, 192 for O-Si-O and Si-O-Si |
| Refinement method | Rietveld refinement |
| R_p , R_{wp} , GoF | 8.85%, 11.52%, 1.92 |

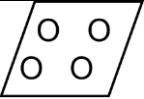
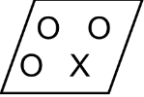
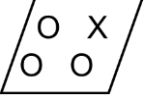
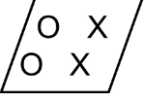
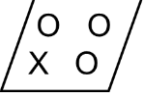
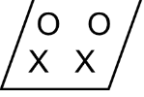
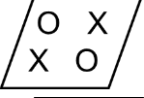
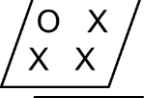
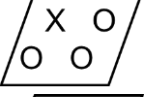
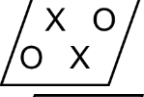
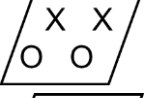
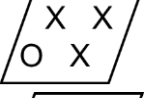
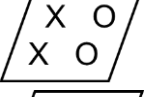
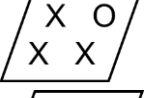
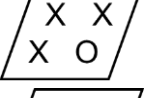
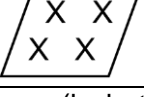
Table S5. Rietveld refined Si-O bond distances (Å) for calcined HPM-18 ($G_{\text{r}} = 0.17$).

| | | | | | |
|---------|----------|----------|----------|----------|----------|
| Si1-O14 | 1.623(8) | Si9-O2 | 1.621(1) | Si17-O38 | 1.654(3) |
| Si1-O2 | 1.601(1) | Si9-O18 | 1.695(2) | Si17-O46 | 1.694(2) |
| Si1-O8 | 1.640(4) | Si9-O27 | 1.660(7) | Si17-O44 | 1.609(1) |
| Si1-O19 | 1.607(2) | Si9-O3 | 1.626(3) | Si17-O47 | 1.676(4) |
| Si2-O1 | 1.688(3) | Si10-O18 | 1.703(1) | Si18-O21 | 1.626(9) |
| Si2-O11 | 1.634(3) | Si10-O23 | 1.591(8) | Si18-O30 | 1.631(1) |
| Si2-O19 | 1.634(5) | Si10-O25 | 1.685(4) | Si18-O37 | 1.628(3) |
| Si2-O6 | 1.637(2) | Si10-O45 | 1.685(1) | Si18-O43 | 1.672(7) |
| Si3-O17 | 1.621(6) | Si11-O10 | 1.609(1) | Si19-O33 | 1.599(3) |
| Si3-O48 | 1.629(3) | Si11-O12 | 1.584(5) | Si19-O38 | 1.645(2) |
| Si3-O5 | 1.611(8) | Si11-O16 | 1.596(3) | Si19-O41 | 1.600(8) |
| Si3-O13 | 1.618(1) | Si11-O7 | 1.630(1) | Si19-O48 | 1.649(9) |
| Si4-O3 | 1.583(8) | Si12-O30 | 1.609(7) | Si20-O32 | 1.582(9) |
| Si4-O17 | 1.607(9) | Si12-O33 | 1.572(9) | Si20-O41 | 1.560(7) |
| Si4-O6 | 1.600(5) | Si12-O28 | 1.598(8) | Si20-O11 | 1.577(5) |
| Si4-O21 | 1.599(3) | Si12-O42 | 1.612(7) | Si20-O37 | 1.592(1) |
| Si5-O13 | 1.622(8) | Si13-O9 | 1.614(1) | Si21-O15 | 1.670(4) |
| Si5-O20 | 1.631(3) | Si13-O22 | 1.597(1) | Si21-O29 | 1.637(4) |
| Si5-O47 | 1.650(6) | Si13-O16 | 1.597(1) | Si21-O35 | 1.639(4) |
| Si5-O25 | 1.651(2) | Si13-O12 | 1.560(2) | Si21-O40 | 1.637(1) |
| Si6-O4 | 1.657(1) | Si14-O26 | 1.619(1) | Si22-O26 | 1.631(6) |
| Si6-O20 | 1.687(2) | Si14-O27 | 1.652(8) | Si22-O40 | 1.613(9) |
| Si6-O24 | 1.690(5) | Si14-O31 | 1.643(5) | Si22-O45 | 1.670(6) |
| Si6-O10 | 1.658(1) | Si14-O32 | 1.598(2) | Si22-O46 | 1.660(9) |
| Si7-O1 | 1.643(2) | Si15-O24 | 1.666(4) | Si23-O22 | 1.613(3) |
| Si7-O4 | 1.611(1) | Si15-O28 | 1.618(1) | Si23-O34 | 1.596(5) |
| Si7-O5 | 1.618(7) | Si15-O36 | 1.606(4) | Si23-O36 | 1.603(3) |
| Si7-O42 | 1.634(1) | Si15-O44 | 1.608(8) | Si23-O39 | 1.605(6) |
| Si8-O8 | 1.628(9) | Si16-O14 | 1.610(6) | Si24-O7 | 1.624(7) |
| Si8-O9 | 1.625(1) | Si16-O43 | 1.636(9) | Si24-O34 | 1.589(6) |
| Si8-O15 | 1.660(9) | Si16-O29 | 1.606(6) | Si24-O35 | 1.604(1) |
| Si8-O23 | 1.590(6) | Si16-O31 | 1.624(4) | Si24-O39 | 1.582(9) |

Table S6. Rietveld refined bond angles (°) for calcined HPM-18 ($G_{\text{r}} = 0.17$).

| Bond angles | Min. | Max. | Average |
|-------------|--------|--------|---------|
| O-Si-O | 105.34 | 113.88 | 109.46 |
| Si-O-Si | 132.96 | 167.47 | 147.81 |

Table S7. Enumeration of the 16 possible ordered polymorphs of HPM-18, their $d4r$ sequences and up and down symbols (columns 1-3), and their topological analysis (columns 4-5), resulting in five topologically different ordered polymorphs and their channel systems (columns 6-7).

| # | $d4r^{[a]}$ | $d4r$ location | Transitivity (V, E, F, T) | Tiling | Polymorph | Channel System ^[b] |
|----|-------------|---|------------------------------|--|-----------|----------------------------------|
| 1 | tttt |  | (96) (192) (126) (30) | $4*[4.5^2.8^2] + 4*[4^6] + [4^2.7^2.10^2] + [4^3.5^4] + [4^3.5^2.12^2] + [4^4.5^4.7^2] + [4^4.5^2.8^4.10^2.12^2] + 2*[4^7.5^6.7^2.8^2.12^2]$ | HPM-18-A | b: 7, 8, 12R c: 10R |
| 2 | tttb |  | (96) (192) (123) (27) | $8*[4.5^2.8^2] + 8*[4^6] + [4^2.7^2.10^2] + [4^3.5^4] + [4^3.5^2.12^2] + [4^4.5^4.7^2] + [4^4.5^2.8^4.10^2.12^2] + 6*[4^7.5^6.7^2.8^2.12^2]$ | HPM-18-B | b: 7, 8, 12R c: 10R |
| 3 | ttbt |  | (96) (192) (123) (27) | Identical to tttb | HPM-18-B | as HPM-18B |
| 4 | ttbb |  | (96) (192) (126) (30) | $4*[4.5^2.8^2] + 4*[4^6] + [4^2.7^2.10^2] + [4^3.5^4] + [4^3.5^2.12^2] + [4^4.5^4.7^2] + [4^4.5^2.8^4.10^2.12^2] + 2*[4^7.5^6.7^2.8^2.12^2]$ | HPM-18-C | b: 7, 8, 12R c: 10R |
| 5 | tbtt |  | (96) (192) (123) (27) | Identical to tttb | HPM-18-B | as HPM-18B |
| 6 | tbtb |  | (96) (192) (120) (24) | $[4.5^2.8^2] + [4^6] + [4^7.5^6.7^2.8^2.12^2]$ | HPM-18-D | b: 7, 8, 12R a,c:undul. 8R |
| 7 | tbbt |  | (96) (192) (120) (24) | $[4.5^2.8^2] + [4^6] + [4^7.5^6.7^2.8^2.12^2]$ | HPM-18-E | b: 7, 8, 12R a,c:undul. 8R |
| 8 | tbbb |  | (96) (192) (123) (27) | Identical to tttb | HPM-18-B | as HPM-18B |
| 9 | bttt |  | (96) (192) (123) (27) | Identical to tttb | HPM-18-B | as HPM-18B |
| 10 | bttb |  | (96) (192) (120) (24) | Identical to tbbt | HPM-18-E | as HPM-18E |
| 11 | btbt |  | (96) (192) (120) (24) | Identical to tbtb | HPM-18-D | as HPM-18D |
| 12 | btbb |  | (96) (192) (123) (27) | Identical to tttb | HPM-18-B | as HPM-18B |
| 13 | bbtt |  | (96) (192) (126) (30) | Identical to ttbb | HPM-18-C | as HPM-18C |
| 14 | bbtb |  | (96) (192) (123) (27) | Identical to tttb | HPM-18-B | as HPM-18B |
| 15 | bbbt |  | (96) (192) (123) (27) | Identical to tttb | HPM-18-B | as HPM-18B |
| 16 | bbbb |  | (96) (192) (126) (30) | Identical to tttt | HPM-18-A | as HPM-18A |

[a] $d4r$ sequence (b, bottom and t, top part of the unit cell along b). [b] Pores are straight unless "undul." (undulating) indicated.

References

- [49] J. D. Gale, "GULP: A computer program for the symmetry-adapted simulation of solids." *J. Chem. Soc., Faraday Trans.* **1997**, 93, 629-637.
- [50] J. D. Gale, A. L. Rohl, "The General Utility Lattice Program (GULP)." *Mol. Simul.* **2003**, 29, 291-341.
- [51] G. Sastre J. Gale, "Derivation of an Interatomic Potential for Fluoride-Containing Microporous Silicates and Germanates", *Chem. Mater.* **2005**, 17, 4, 730–740
- [52] S. L. Mayo *et al.*, "DREIDING: a generic force field for molecular simulations", *J. Phys. Chem.* **1990**, 94, 26, 8897–8909.
- [53] a) A. K. Rappe & W. A. Goddard III, "Charge equilibration for molecular dynamics simulations", *J. Phys. Chem.*, **1991**, 95, 3358-3363, b) A. Nakano, "Parallel multilevel preconditioned conjugate-gradient approach to variable-charge molecular dynamics", *Comp. Phys. Comm.*, **1997**, 104, 59-69, c) S. W. Rick, S. J. Stuart, B. J. Berne, "Dynamical fluctuating charge force fields: Application to liquid water", *J. Chem. Phys.*, **1994**, 101, 16141.
- [54] R. Grau-Crespo, S. Hamad, C. R. A. Catlow, N. H. de Leeuw, "Symmetry-adapted configurational modelling of fractional site occupancy in solids", *J. Phys. Condens. Matter* **2007**, 19, 256201.
- [55] R. Grau-Crespo, U. V. Waghmare in *Molecular Modeling for the Design of Novel Performance Chemicals and Materials*, (Ed.: B. Rai), CRC Press, **2012**, ch. 11.
- [56] R. T. Rigo *et al.*, "The Si–Ge substitutional series in the chiral STW zeolite structure type" *J. Mater. Chem. A*, **2018**, 6, 15110-15122.
- [57] J. Arce-Molina, R. Grau-Crespo, D. W. Lewis, A. R. Ruiz-Salvador, "Screening heteroatom distributions in zeotype materials using an effective Hamiltonian approach: the case of aluminogermanate PKU-9", *Phys. Chem. Chem. Phys.*, **2018**, 20, 18047-18055.